J. Korean Earth Sci. Soc., v. 45, no. 4, p. 292–303, August 2024
https://doi.org/10.5467/JKESS.2024.45.4.292
ISSN 1225-6692 (printed edition)
ISSN 2287-4518 (electronic edition)

Numerical Simulation of Quasi-Spherical, Supersonic Accretion Flows - Code and Tests

Siek Hyung and Seong-Jae Lee*

Department of Earth Science Education, Chungbuk National University, Chungbuk 28644, Korea

Abstract: We study quasi-spherical, supersonic accretion flows around black holes using high-accuracy numerical simulations. We describe a code, the Lagrangian Total Variation Diminishing (TVD), and a remap routine to address a specific issue in the Advection Dominated Accretion Flow (ADAF) that is, appropriately handling the angular momentum even near the inner boundary. The Lagrangian TVD code is based on an explicit finite difference scheme on mass-volume grids to track fluid particles with time. The consequences are remapped on fixed grids using the explicit Eulerian finite-difference algorithm with a third-order accuracy. Test results show that one can successfully handle flows and resolve shocks within two to three computational cells. Especially, the calculation of a hydrodynamical accretion disk without viscosity around a black hole shows that one can conserve nearly 100% of specific a ngular momentum in one-and two-dimensional cylindrical coordinates. Thus, we apply this code to obtain a numerically similar ADAF solution. We perform simulations, including viscosity terms in one-dimensional spherical geometry on the non-uniform grids, to obtain greater quantitative consequences and to save computational time. The error of specific angular momentum in Newtonian potential is less than 1% between r~$10r_s$ and r~10^4r_s, where r_s is sink size. As Narayan et al. (1997) suggested, the ADAFs in pseudo-Newtonian potential become supersonic flows near the black hole, and the sonic point is r_{sonic}~$5.3r_g$ for flow with α=0.3 and γ=1 .5. Such simulations indicate that even the ADAF with γ=5/3 is differentially rotating, as Ogilvie (1999) indicated. Hence, we conclude that the Lagrangian TVD and remap code treat the role of viscosity more precisely than the other scheme, even near the inner boundary in a rotating accretion flow around a nonrotating black hole.

Keywords: accretion disks-hydrodynamics-methods: numerical simulation

1. Introduction

One of the most important aspects of numerical simulations is minimizing numerical errors due to code. Many studies have been done for several years, and many kinds of schemes have been developed to reduce numerical errors. Of those schemes, high-order, conservative, upwind differencing schemes have proven very efficient in solving compressible hydrodynamic equations. These methods based on the so-called Rieman solution generally depend on estimating mass, momentum, and energy fluxes across cell boundaries. Several examples include Godunov's scheme (Godunov 1959), MUSCL scheme (Van Leer 1979), Roe Scheme (Roe 1981), TVD scheme (Harten 1983), PPM scheme (Collella & Woodward 1984), ENO scheme (Harten et al. 1987) and WENO (Liu et al. 1994; Jiang & Shu 1996).

Meanwhile, numerical simulations to solve compressible hydrodynamic equations with viscosity terms were performed by Igumenshchev et al. (1996) and Igumenshchev & Abramowicz (1999 & 2000). They mainly examined the features of Advection Dominated Accretion Flow (ADAF). The code work must follow up angular momenta more accurately, even close to the inner boundary, to study the features of ADAF near the edge of a black hole. Most of the angular momentum is transferred outwards near the inner region, and the flow is absorbed in a black hole. Especially the conservation of angular momenta in curved geometrical coordinates has been one of the issues to be solved in the Eulerian scheme since azimuthal momentum equations are not easy to

*Corresponding author: seong@chungbuk.ac.kr
Tel: +82-43-261-2726

This is an Open-Access article distributed under the terms of the Creative Commons Attribution Non-Commercial License (http://creativecommons.org/licenses/by-nc/3.0) which permits unrestricted non-commercial use, distribution, and reproduction in any medium, provided the original work is properly cited.

decouple from the rest of the equations. In addition to this, since both boundary conditions influence the numerical calculation, including viscosity terms, caution must be applied to follow up on angular momenta accurately. Therefore, we have built a code that implements Lagrangian Total Variation Diminishing (TVD) scheme and remapping to reduce the errors in calculating the angular momentum.

Lagrangian TVD scheme consists of Lagrangian and TVD schemes: the former is a scheme to track a particular fluid particle with time, while the latter is a Diminishing Total Variation that is designed by Ryu et al. (1995a; 1995b; 1995c) based on Harten (1983). Since the azimuthal momentum equation in the Lagrangian scheme is decoupled from the rest of the equations, it is believed to be very efficient in conserving angular momenta. TVD scheme was known to resolve shocks within a few cells, e.g., two to four cells. Hence, we have built up the Lagrangian TVD to obtain two strong points: (1) the Lagrangian method can follow angular momentum as accurately as possible, and (2) the TVD scheme can detect shocks sharply. This paper will show that the Lagrangian TVD and remap code help conserve the angular momentum in Eulerian equations. Furthermore, the code can be drawn well the analytical self-similar solutions of ADAF because the viscosity terms in azimuthal momentum equations are treated separately using an implicit method.

In §2, we introduce the implementation of Lagrangian TVD and remap code, including the operator splitting, to answer the needs of people who do numerical calculations. We describe the process of building up the Lagrangian TVD code in detail, in which the results are mapped into fixed points by remap routine with high order accuracy. We will show that the code can correctly handle the nature of hydrodynamical flows, capturing shocks and contact discontinuities through the shock tube test. Moreover, we will simulate the rotating flow around a black hole where the accretion shock is formed to see how accurately this code can conserve angular momentum in one and two-dimensional cylindrical geometry. We will investigate the differences between the results from Lagrangian TVD and remap with those by Molteni et al. (1996, hereafter, MRC96) with the same initial conditions. In §3, we describe the time-dependent equations of ADAFs based on Narayan & Yi (1994, hereafter, NY94) and compare the consequences from the numerical simulation with the analytical self-similar solutions derived from the equations at steady state. We will show that the code can draw the analytical self-similar solution well by following up the angular momentum. Summary and Discussions are given in §4.

2. Numerical Scheme and Test Results

In this section, we explain the process of constructing the Lagrangian TVD and remap. To see the conservation of angular momentum, test results in one and two-dimensional cylindrical geometries are shown in uniform grid cells. Especially, we describe the construction of non-uniform grids: the calculation with viscosity terms was made on the non-uniform grids, which is believed to be very efficient in reducing the computing time.

2.1. One-Dimensional Hydrodynamical Equations for Lagrangian TVD

We describe the hydrodynamical evolution with equations in which the effects of cooling and heating are ignored. In multi-dimensional geometry, the ideal hydrodynamical equations by Collella & Woodward (1984) are written in a conservative form as follows:

$$\frac{\partial \tau}{\partial t} - \frac{\partial (r^{\beta} v)}{\partial m} = 0 \tag{1}$$

$$\frac{\partial v}{\partial t} + r^{\beta} \frac{\partial p}{\partial m} = 0 \tag{2}$$

$$\frac{\partial E}{\partial t} + \frac{\partial (r^{\beta} v p)}{\partial m} = 0 \tag{3}$$

where the state vectors, τ, v and E are a specific volume, a radial velocity and a total energy per unit volume, respectively. The density ρ, the internal energy e and the pressure p are to be derived from conserved quantities via

$$\rho = 1/\tau, \quad e = E - v^2/2, \quad p = (\gamma - 1)\rho e \tag{4}$$

where v, p and vp are the flux functions. The pressure, $p = \frac{1}{\gamma\tau}c_s^2$, where c_s is the adiabatic sound speed. The spatial distance r in a coordinate is related to a mass m via

$$m(r) = \int_{r_0}^{r} \rho(r) r^{\beta} dr \tag{5}$$

where $\beta = 0,\ 1,\ 2$ are planar, cylindrical, or spherical symmetry, respectively depending on the cases. The function $r\,(m,\, t)$ satisfies the ordinary differential equation $dr/dt = v\,(m,\, t)$.

2.2. One-Dimensional Functioning Code and Remap

We consider the planar geometry, that is, the case of $\beta = 0$. The first step to build a one-dimensional function is to find eigenvalues, the right and left eigenvectors of Jacobians **A**(**q**). Three eigenvalues of **A**(**q**) are in non-increasing order

$$a_1 = -\frac{c_s}{\tau}, \quad a_2 = 0, \quad a_3 = \frac{c_s}{\tau}. \tag{6}$$

The quantities a_1, a_2, and a_3 represent the three speeds whose information is propagated by hydrodynamic wave and entropy mode. The following eigenvectors are found from the Jacobian matrix of the system of Eqs. (1)-(3).

$$R_1 = \begin{pmatrix} 1 \\ \frac{c_s}{\tau} \\ -\frac{c_s^2}{\gamma\tau} + \frac{c_s \nu}{\tau} \end{pmatrix}, \quad R_2 = \begin{pmatrix} 1 \\ 0 \\ \frac{1}{\gamma(\gamma-1)}\frac{c_s^2}{\tau} \end{pmatrix},$$

$$R_3 = \begin{pmatrix} 1 \\ -\frac{c_s}{\tau} \\ -\frac{c_s^2}{\gamma\tau} - \frac{c_s \nu}{\tau} \end{pmatrix} \tag{7}$$

The left eigenvectors, which are orthonormal to the right eigenvectors, $L_l \cdot R_m = \delta_l m$ are

$$L_1 = \left(\frac{1}{2\gamma},\ \frac{\tau}{2c_s} + \frac{(\gamma-1)\tau\nu}{2c_s^2},\ -\frac{(\gamma-1)\tau}{c_s^2}\right) \tag{8}$$

$$L_2 = \left(\frac{(\gamma-1)}{\gamma},\ -\frac{(\gamma-1)\tau\nu}{c_s^2},\ \frac{(\gamma-1)\tau}{c_s^2}\right) \tag{9}$$

$$L_3 = \left(\frac{1}{2\gamma},\ -\frac{\tau}{2c_s} + \frac{(\gamma-1)\tau\nu}{2c_s^2},\ -\frac{(\gamma-1)\tau}{c_s^2}\right) \tag{10}$$

The fluxes in the Lagrangian TVD is built using eigenvalues and eigenvectors with flow quantities at the cell center. First of all, the $m(r)$-flux is calculated using the one-dimensional functioning code, where the mass $m(r)$ in a coordinate is related to a spatial distance r as in Eq. (5). In calculating the $m(r)$-flux, we define an updated state vector which includes the effects of the source terms at each time step as follows:

$$q_i^{n+1} = q_i^n - \frac{\Delta t^n}{\Delta x}(f_{i+\frac{1}{2}} - f_{i-\frac{1}{2}}) \tag{11}$$

Fluxes in m(r)-coordinate are calculated as follows:

$$f_{i+\frac{1}{2}} = \frac{1}{2}[F(q_i^n) + F(q_{i+1}^n)] - \frac{\Delta x}{2\Delta t^n}\sum_{k=1}^{2}\beta_{k,i+\frac{1}{2}} R^n_{k,i+\frac{1}{2}}, \tag{12}$$

$$F(q^n_{i+\frac{1}{2}}) = \frac{F(q_i^n)\Delta m_{i+1} + F(q_{i+1}^n)\Delta m_i}{\Delta m_{i+1} + \Delta m_i}, \tag{13}$$

$$\Delta m_{i+\frac{1}{2}} = \frac{2\Delta m_{i+1}\Delta m_i}{\Delta m_{i+1} + \Delta m_i}, \tag{14}$$

$$\beta_{k,i+\frac{1}{2}} = Q_k\left(\frac{\Delta t^n}{\Delta x} a^n_{k,i+\frac{1}{2}} + \gamma_{k,i+\frac{1}{2}}\right)\alpha_{k,i+\frac{1}{2}} - (g_{k,i} + g_{k,i+1}), \tag{15}$$

$$\alpha_{k,i+\frac{1}{2}} = L^n_{k,i+\frac{1}{2}}(q^n_{i+1} + q^n_i), \tag{16}$$

$$\gamma_{k,i+\frac{1}{2}} = \begin{cases} \dfrac{g_{k,i+1} - g_{k,i}}{\alpha_{k,1+\frac{1}{2}}} & \text{for} \quad \alpha_{k,i+\frac{1}{2}} \neq 0, \\ 0 & \text{for} \quad \alpha_{k,i+\frac{1}{2}} = 0, \end{cases} \tag{17}$$

$$g_{k,i} = \mathrm{sign}(\tilde{g}_{k,i+\frac{1}{2}})\max[0, \min\{|\tilde{g}_{k,i+\frac{1}{2}}|, 2\mathrm{sign}(\tilde{g}_{k,i-\frac{1}{2}})\}, \min\{2|\tilde{g}_{k,i+\frac{1}{2}}|,\ \mathrm{sign}(\tilde{g}_{k,i-\frac{1}{2}})\}], \tag{18}$$

$$g_{k,i}=\mathrm{sign}(\tilde{g}_{k,i+\frac{1}{2}})\max[0,\ \min\{|\tilde{g}_{k,i+\frac{1}{2}}|,\ \mathrm{sign}(\tilde{g}_{k,i-\frac{1}{2}})\}], \tag{19}$$

$$g_{k,i}=\mathrm{sign}(\tilde{g}_{k,i+\frac{1}{2}})\max[0,\ \min\{|\tilde{g}_{k,i+\frac{1}{2}}|+\mathrm{sign}(\tilde{g}_{k,i-\frac{1}{2}})\},$$
$$\{2|\tilde{g}_{k,i+\frac{1}{2}}|,\ 2\mathrm{sign}(\tilde{g}_{k,i-\frac{1}{2}})\}], \tag{20}$$

$$\tilde{g}_{k,i+\frac{1}{2}}=\frac{1}{2}\left[Q_k\left(\frac{\Delta t^n}{\Delta x}a^n_{k,i+\frac{1}{2}}\right)-\left(\frac{\Delta t^n}{\Delta x}a^n_{k,i+\frac{1}{2}}\right)^2\right]\alpha_{k,i+\frac{1}{2}}, \tag{21}$$

$$Q_k(\chi)=\begin{cases}\dfrac{\chi^2}{4\varepsilon}+\varepsilon, & \text{for} \quad |\chi|<2\varepsilon,\\ |\chi|, & \text{for} \quad |\chi|\geq 2\varepsilon,\end{cases} \tag{22}$$

$$\varepsilon=0.3 \tag{23}$$

Equation (18) is a superbee flux limiter of high-resolution limiters in the Lagrangian TVD scheme. The idea of the flux limitation is to reduce the magnitude of a numerical flux to avoid oscillation near a discontinuity. In addition to Eq. (18), we have tested the code with two more flux limiters which are minmode and monotonized central- difference limiter (MC-flux limiter). The former method is to compare the two slopes and to choose the smaller one in magnitude. The code has been tested with Eq. (19) for the minmode flux limiter. The latter is sharpening the resolution of discontinuities which may be achieved with other limiters as in Eq. (20) that does not reduce the slope as severely as minmod near a discontinuity.

Since the above Eqs. (1)-(3) are integrated by Lagrangian TVD which tracks fluid particle variation with time, the density, radial velocity, and energy in Lagrangian coordinates are remapped onto a fixed Eulerian coordinate. At the beginning of Lagrangian step, the Lagrangian and Eulerian zones coincide. After a Lagrangian step, the Lagrangian zone moves to the updated coordinate with flow velocity v_r as follows:

$$\xi_i=\xi_o+v_r\Delta t \tag{24}$$

where ξ_i is in a new coordinate of the Lagrangian zone boundary, while ξ_o is in an old coordinate of the Lagrangian zone boundary. The Lagrangian zone coincides with the Eulerian zone after the Lagrangian zone has shifted with updated distribution $v_r\Delta t$. All the interpolations for remap have been performed in the volume coordinate $r^{\beta+1}/(\beta+1)$ with the third-order accuracy, e.g., $\beta=0$, 1, and 2 for planar, cylindrical, and spherical geometry (Collella & Woodward 1984). The calculation has been performed on the uniform grids for the hydrodynamical steps, in which the grid size is constant and relatively small for high resolution, whereas on the non-uniform grids for the equations of ADAF, the grid size increases exponentially and is set as follows:

$$dr(i)=dr(1)\times b^{(i-1)} \tag{25}$$

$$r(i)=dr(i)\times(b^i-1)/(b-1), \tag{26}$$

where $dr(i)$ is the grid size of i^{th} cell, $dr(1)$ is the first grid size, b is the increment factor and $r(i)$ is the distance of the i^{th} cell from the center. Since grid sizes increase exponentially, small grid sizes near the inner boundary can get more accurate results, while bigger grid sizes near the outer boundary can make long-length box sizes with fewer grid cells. Tests showed that since the calculation for ADAF requires high resolution in uniform grids to get better numerical results, it takes a very long time to reach the steady state. To save the computational time and to get the qualitative results, our calculation has been done on a non-uniform grid with only 780 cells to achieve the same resolution as was possible with more than 12000 cells in uniform grids of the same box size. Especially, the non-uniform grids are very useful for numerical simulation to calculate the equations which include viscosity terms because they allow us to see the high-resolution effects of calculating angular momentum around a black hole.

2.3. Two-Dimensional Hydrodynamical Step for Cylindrical Geometry

Two-dimensional code can be decomposed into one-dimensional functioning codes through a Strang-type directional splitting (Strang 1968). For two-dimensional cylindrical coordinate, the calculation of r-path has

been done on the cylindrical coordinate, while the calculation of z-path has been done on the plane parallel coordinate (Ryu et al. 1995a & 1995b for detail).

When the calculation has been done on the cylindrical coordinate for $\beta = 1$, or one-dimensional spherical geometry for $\beta = 2$, the azimuthal momentum equation is decoupled from Eqs. (1)-(3), respectively. So, it is possible to handle separately and to conserve the angular momentum accurately as follows:

$$\frac{dl}{dt} = 0 \tag{27}$$

where, $\frac{d}{dt} = \frac{\partial}{\partial t} + v_r \frac{\partial}{\partial r}$.

If there are external forces such as gravity, the momentum and energy equations will have source terms, i.e., g in Eq. (2) and vg in Eq. (3). Since self-gravitation of flow is neglected and g is a body force depending on r, $g \equiv \frac{\partial \Phi}{\partial r}$ and $\Phi = -\frac{GM}{r}$ in Newtonian potential, whereas $\Phi = -\frac{GM}{(r - r_g)}$ in Paczynsky & Wiita potential (1980) with Schwarzschild radius r_g. If the calculation has been done on a lower-dimension using cylindrical or spherical symmetry, the equations must also include geometric source terms.

The source terms were solved in a source treatment step using fractional step (splitting) methods, in which the problem is split into pieces corresponding to the different processes and a numerical method appropriate for each separate piece is applied independently. We used the implicit method to solve the source terms in one-dimensional geometry, while we used the explicit method in two-dimensional cylindrical geometry.

2.4. Shock Tube Test

The first step intends to mimic the shock tube test. We have tested in a computational box size (=1), with γ=5/3, Courant constant C_{cour}=0.8 and ε=0.1. Figure 1 shows three distinct waves in separating regions with $\rho_l = p_l$=3 and $\rho_r = p_r$=1. A shock wave propagates into the region of lower pressure, across the region of which the density and pressure jump to higher values and all of the state variables are discontinuous. We used a superbee flux limiter, in which shock could resolve more sharply than the other flux limiters, e.g., minmode and MC-flux limiter. A contact discontinuity, across the region of which the density is again discontinuous but the velocity and pressure are constant. To detect the contact discontinuity within a few cells, we refined or turned on stiffness in a remap routine which could handle entropy mode. The third wave is called a rarefaction wave since the density of the gas is rarefied; all of the state variables are continuous and there is a smooth transition (LeVeque 1998). While the straight lines represent the analytical solutions, the circles show the test results of pressure, density, and radial velocity at the time step of t=0.2 with 1024 grid cells.

2.5. One-Dimensional Accretion Shock

In a second test, we check the degree of shock capture activity when the rotating flow is approaching to the centrifugal barrier in a one-dimensional cylindrical geometry. Thus, we assume a thin, rotating, adiabatic accretion flow near the nonrotating central compact object with Paczynski & Wiita (1980) potential. For a complete solution of the stationary model, the equations of energy, momentum, and mass conservation are necessary. In the case of axisymmetric flow without viscosity, the azimuthal momentum equation conserves specific angular momentum at steady state, $\frac{dl}{dt}$=0. Since the equation for the azimuthal momentum can be decoupled from the rest of the equations, we can treat it separately.

Figure 1 of Lee et al. (2011), which used this code, compares analytical and numerical results in a one-dimensional accretion flow with a standing shock. The inflow with (ρ, p, v_r, l) = (1, 0.0105886, −0.083566, 1.8) is set at the outer boundary and adiabatic index of γ=4/3. The flow is pulled by the gravitational force of a black hole only at the center of the box and it is sucked by the sink area, which occupies a space of 3 % or less of the box size. Density and Mach number are plotted in 2048 grid cells. The solid curves are the analytical solutions, while the circles represent our

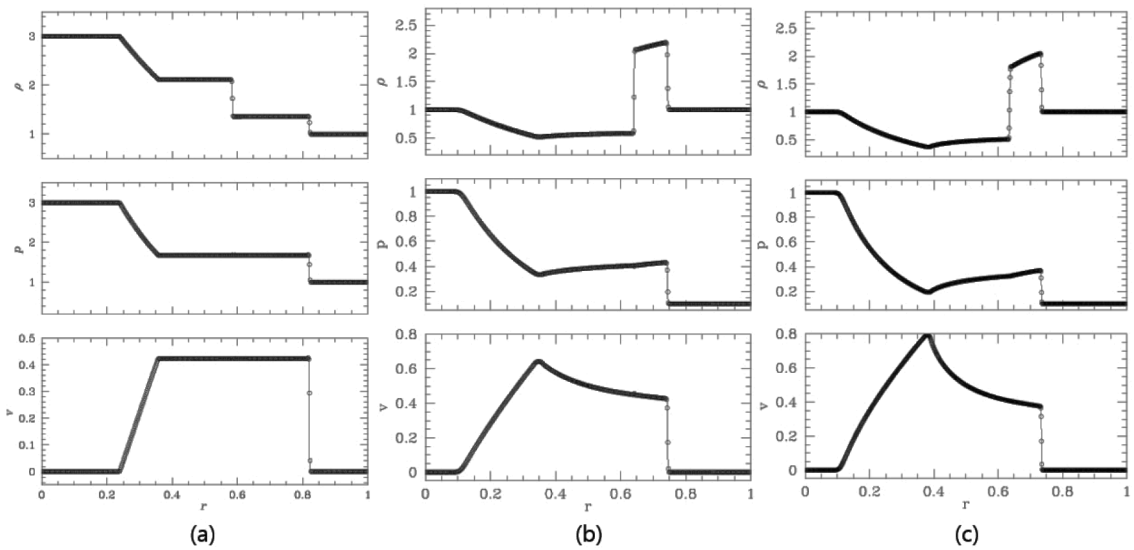

Fig. 1. Shock tube test. Plots show density (ρ), pressure (p), and radial velocity (v) from the top. (a), (b), and (c) are the results of plane parallel and cylindrical and spherical geometry for β=0, 1, and 2, respectively. The straight lines show the analytical solutions, while the open circles represent the results from the code test. The calculation has been done on 512 uniform grid cells using the superbee flux limiter. The shock is resolved sharply with 2-3 grid cells.

code simulation results. Note that the shock is captured nicely within 2 to 3 cells and the results coincide with the analytical solution fairly well [Fig. 1 of MRC96 for comparison].

2.6. Two-Dimensional Accretion Shock

To see the case of two-dimensional cylindrical geometry which is constructed by the operator Strang-type splitting method (Strang 1968), we have tested a standing shock case in accretion flow as in the above case. MRC96 pointed out that the shock structure on the equatorial plane is different in Eulerian TVD and SPH code because Eulerian TVD has a few percent of errors in angular momentum [Fig. 3a of MRC96]. Hence, to search for shock structures of the equatorial plane, we have run the code with the same initial condition as in MRC96, e.g., $v_r = -0.068212$, sound speed c_s=0.061463, adiabatic index γ=4/3 and specific angular momentum l=1.65. The matter is supplied from an outer boundary and is absorbed at the inner edge in the same way as in the one-dimensional case.

Figure 2 shows the density contour and velocity fields in the r-z plane. The calculation has been done with 128×256 cells in a 50×100 box size. The contour level of the minimum density is 0.0261. Successive contours have a density ratio of 1.2. The consequences show a clear presence of the funnel wall. They show the presence of an oblate spheroidal shock near the equatorial plane. The shock touches the equatorial plane roughly at r~24. The inner solid curve is the location of the funnel wall that is the surface of vanishing effective potential, while the outer solid curve is a centrifugal barrier that is governed by the competition between the centrifugal force and gravitational force.

When we compare Fig. 2 with Figs. 3a & 3b of MRC96, the density contour map is similar to Fig. 3(b) of MRC96. It has one shock structure because the code uses Lagrangian scheme and remap like SPH code in which the specific angular momentum conserves strictly. However, the shock position is similar to Fig. 3(a) of MRC96 because our code used TVD method in which the shock is resolved sharply.

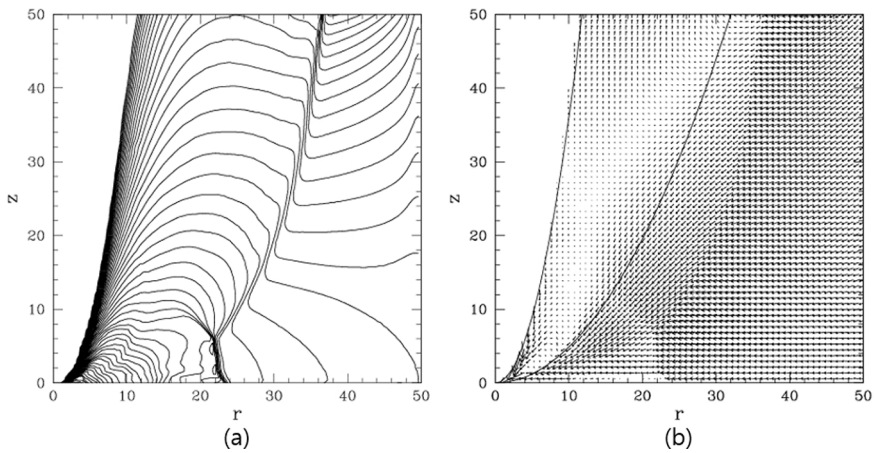

Fig. 2. Density contours and velocity fields in the r-z plane. The big paraboloidal accretion shock touches in the equatorial plane, at r~24. To compare the results to Figs. 3(a) and 3(b) of MRC96, we used the same initial condition as MRC96 in 128×256 uniform grid cells. The locations of the funnel wall (inner curve) and the centrifugal barrier (outer curve) are superimposed by solid curves, respectively.

3. Application to Advection Dominated Accretion Flow

The viscosity in rotating accretion flows has two effects. First, it redistributes angular momentum so that some of the matter spread outwards carrying angular momentum out. As a result, it allows the rest of the matter to spiral inwards (Pringle 1981). At the same time, the viscosity acts as a frictional force, which results in the dissipation of heat (Longair 1994). Unfortunately, it is very difficult to display the structure which visualizes the precise role of viscosity through numerical simulation, especially, near the inner edge of the black hole because the numerical calculations with viscosity terms would be affected by boundary conditions. Moreover, it requires a higher resolution near the inner boundary to get better results, so it requires too much computational time to reach the steady state. However, we have solved these problems by using the continuous boundary conditions and non-uniformly or exponentially increasing grid size.

3.1. Time Dependent Equations of ADAF

In the last test, we apply this code to ADAF in which most of the viscously dissipated energy is stored as an entropy rather than being radiated. Assuming an axisymmetric flow where the temperature of the accreting gas is nearly virialized and the flow structure is quasi-spherical, the time-dependent equations for ADAF have been derived from NY94. When the self-gravitation of gas is ignored, the gas density ρ, its radial velocity v, angular velocity Ω and adiabatic sound speed c_s, satisfy the following four differential equations, namely the continuity equation, the radial and azimuthal components of the momentum equation, and the energy equation;

$$\frac{\partial \rho}{\partial t}+\frac{1}{r^{\beta}}\frac{\partial}{\partial r}(r^{\beta}\rho v)=0 \tag{28}$$

$$\frac{\partial(\rho v)}{\partial t}+\frac{1}{r^{\beta}}\frac{\partial(r^{\beta}\rho v^{2})}{\partial r}=\rho\frac{l^{2}}{r^{3}}-\rho g-\frac{\partial p}{\partial r} \tag{29}$$

$$\frac{dl}{dt}=rq_{\varphi} \tag{30}$$

$$\frac{\partial \varepsilon}{\partial t}+\frac{1}{r^{\beta}}\frac{\partial(r^{\beta}(\varepsilon+p)v)}{\partial r}=F_{\varphi}-\rho g v \tag{31}$$

where, q_{φ} is the viscous force just for the azimuthal direction and derived from Igumenschev et al. (1996) based on Tassoul (1978),

$$q_{\varphi}\approx\frac{1}{r}\frac{\partial}{\partial r}(r\tau_{\varphi r})\,. \tag{32}$$

The viscous stress tensor component is $\tau_{\varphi r} = 2\mu D_{r\varphi}$, while the shear tensor component is $D_{r\varphi} = \frac{r}{2}\frac{\partial}{\partial r}\left(\frac{l}{r^2}\right)$. μ is a dynamical viscosity coefficient, which is described by the α prescription based on Sakura & Sunyaev (1973),

$$\mu = \alpha\rho\frac{c_s^2}{\Omega_K}. \tag{33}$$

Generally, α is a constant and less than 1. Since we assume an axisymmetric flow, $\frac{\partial}{\partial\phi} = 0$, we denote the gas pressure as $p = \frac{\rho}{\gamma}c_s^2$, the Keplerian angular velocity as $\Omega_K(r) = \left(\frac{GM}{r^3}\right)^{\frac{1}{2}}$ in Newtonian potential, whereas $\Omega_K(r) = \left(\frac{GM}{(r-r_g)^2 r}\right)^{\frac{1}{2}}$ in pseudo-Newtonian potential. The heat dissipation function in flux form is defined as follows:

$$F_\varphi \equiv \frac{1}{r^\beta}\frac{\partial}{\partial r}\left(r^\beta r\mu v_\theta \frac{\partial}{\partial r}\left(\frac{v_\theta}{r}\right)\right). \tag{34}$$

Meanwhile, the following internal energy equation satisfies the total energy Eq. (31).

$$\frac{\partial(\rho e)}{\partial t} + \frac{1}{r^\beta}\frac{\partial}{\partial r}(r^\beta \rho e v) + \frac{p}{r^\beta}\frac{\partial}{\partial r}(r^\beta v) = Q^+ - Q^-$$
$$\equiv f\mu r^2\left(\frac{\partial\Omega}{\partial r}\right)^2. \tag{35}$$

Here, e is the specific internal energy. The middle part of the Eq. (35) means the difference between the energy input per unit area due to viscous dissipation (Q^+) and the energy loss through radiative cooling (Q^-) and those are defined as the right-hand side of Eq. (35) based on NY94. f is 1 for considering non-radiative cooling flow only, whereas f will be less than 1 for assuming radiative cooling. If the flow reaches a steady state, Eqs. of (28)-(31) become those of NY94 because $\frac{\partial}{\partial t}$ is zero.

For the numerical integration of the above Eqs. (28)-(31), we divided them into two sub-steps: hydrodynamical and viscous steps. The hydrodynamical sub-step is calculated by using the Lagrangian TVD and remap routine on one-dimensional spherical geometry with β=2. Since the viscous sub-step of Eq. (30) is a system of linear equations and it has nonzero components, the equation has been transformed into the following three vectors using an implicit method in a non-uniform grid;

$$a_i l_{i-1}^n + b_i l_i^n + c_i l_{i+1}^n = -a_i l_{i+1}^o - (b_i - 2) l_i^o - c_i l_{i+1}^o \tag{36}$$

$$a_i = -K_i \mu_{i-\frac{1}{2}} r^3_{i-\frac{1}{2}} \frac{1}{\Delta r_{i-\frac{1}{2}}} \frac{1}{r^2_{r-1}} \tag{37}$$

$$b_i = K_i \mu_{i+\frac{1}{2}} r^3_{i+\frac{1}{2}} \frac{1}{\Delta r_{i+\frac{1}{2}}} \frac{1}{r_i^2} + K_i \mu_{i-\frac{1}{2}} r^3_{i-\frac{1}{2}} \frac{1}{\Delta r_{i-\frac{1}{2}}} \frac{1}{r_i^2} + 1 \tag{38}$$

$$c_i = -K_i \mu_{i+\frac{1}{2}} r^3_{i+\frac{1}{2}} \frac{1}{r^2_{i+1}} \frac{1}{\Delta r_{i+\frac{1}{2}}} \tag{39}$$

where, l_i^n is an updated specific angular momenta in i^{th} cell, while l_i^o is former specific angular momenta in i^{th} cell. Also, μ_i and K_i are defined as follows;

$$\mu_i \equiv \frac{\alpha\rho_i c_{si}^2 r_i}{\Omega_K} \tag{40}$$

$$K_i \equiv \frac{1}{2}\frac{1}{\rho_i r_i^2}\frac{\Delta t}{\Delta r_i} \tag{41}$$

The above linear Eq. (36) is tridiagonal, that is, has nonzero elements only on the diagonal plus or minus one column. To get the updated specific angular momentum, we used a subroutine given by Press et al. (1992) to solve the tridiagonal matrix. Meanwhile, the viscously generated energy Q in Eq. (35) is calculated explicitly.

3.2. Analytical Self-Similar Solutions of ADAF

Based on NY94, we obtained the analytical self-similar solution from the Eqs. (28)-(31) at the steady state with adiabatic sound speed as follows:

$$v = -\frac{2\varepsilon' + 5}{3\alpha\gamma} g(\alpha, \varepsilon')\, v_K \tag{42}$$

$$c_s = \left[\frac{2(2\varepsilon' + 5)}{9\alpha^2\gamma} g(\alpha, \varepsilon')\right]^{\frac{1}{2}} v_K \tag{43}$$

$$\Omega=\left[\frac{2\varepsilon'(2\varepsilon'+5)}{9\alpha^2\gamma^2}g(\alpha,\varepsilon')\right]^{\frac{1}{2}}\Omega_K \tag{44}$$

$$g(\alpha,\varepsilon')\equiv\left[1+\frac{18\alpha^2\gamma^2}{(2\varepsilon'+5)^2}\right]^{\frac{1}{2}}-1 \tag{45}$$

where v_K is Keplerian velocity $v_K=(GM/r)^{\frac{1}{2}}$ Since we consider non-radiative cooling flow only, we have $f=1$, $\varepsilon=(\frac{5}{3}-\gamma)/(\gamma-1)$ and $\varepsilon'\equiv\varepsilon/f=\varepsilon$. Note that the angular velocity is zero for $\gamma=5/3$ based on the Eq. of (44).

3.3. Boundary Conditions and Inflow

The numerical simulation in Newtonian potentials has been performed in a calculation domain which is located $0\le r\le 3$. This corresponds to $r=0r_s-10^5r_s$, where r_s is a sink size which corresponds to about 3 cells, $r_s=2\times10^{-5}$. We have used nonhomogeneous grids with about 780 cells. The first size of the grid is 1.3×10^{-5} and the increment factor is 1.01. However, we have used about 490 nonhomogeneous grid cells for the calculation in Paczynski & Witta (1980) potentials because flows in pseudo-Newtonian potential are supersonic flows close to the edge of a black hole. And it requires longer computational time to reach the steady state than in Newtonian potentials. Therefore, the computational domain has been set differently from the former: the first size of grid is 2.4×10^{-4} and the sink size is 4×10^{-4}. The Schwarzschild's radius r_g is $4/3\times10^{-4}$. The increment factor is 1.01. Hence, the calculation domain corresponds to $0-10^4r_g$.

We used the sucking inner boundary condition in which the flow passes through the inner boundary freely and there is a negligible influence on the pressure from the inner layers. The outer boundary condition should allow the possibility of both outflow and inflow through the outer boundary. However, in order to reduce the error due to the dual effect of the outer boundary, we selected the continuous outer boundary which allows the possibility of outflow only.

The inflow is steadily injected into the calculation domain from the position of r~0.95–0.99, which corresponds to $\sim5\times10^4r_s$ for Newtonian potentials, whereas it corresponds to $\sim5\times10^3r_g$ for pseudo-Newtonian potentials. Here, we assume that the supplying matter is coming from an equatorial torus with Gaussian density distribution and the torus has Keplerian angular velocity since the position of the torus is the place where the centrifugal force is balanced by the gravitational force. Due to the viscous effect, some of the injected flow will lose angular momentum and move inwardly, forming an accretion flow. Another part of inflow with acquired angular momentum moves outwardly. After a while, the accretion flow achieves a quasi-stationary condition and finally, reaches a steady state. Since these flows show persistent stability, chaotic fluctuations do not appear anymore with time at any given point.

3.4. Numerical Results

Figure 2 of Lee et al. (2011), which used this code, shows density (top left), radial velocity & sound speed (top right), pressure (bottom left) and specific angular momentum (bottom right) in Newtonian potential. The sound speed and the radial velocity are shown in the unit of Keplerian velocity in the position of sink $v_K(r_s)$, while the specific angular momentum is shown in the unit of Keplerian specific angular momentum in the position of sink $l_K(r_s)$. The straight lines of density and pressure match on $\rho\propto r^{-\frac{3}{2}}$ and $p\propto r^{-\frac{5}{2}}$. The straight lines for radial velocity, sound speed, and specific angular momentum are the analytical self-similar solutions from the Eqs. of (42)-(45). The dotted points are the consequences of the numerical simulation. The physical parameters used in this simulation are $\alpha=0.3$, $\gamma=4/3$ and $f=1$. Since the azimuthal component of the momentum equation is separately treated in this code, it has a strong advantage in solving the angular momentum accurately to minimize the errors even near the edge of a black hole. The error of specific angular momentum is less than 1 % between r~$10r_s$ and r~10^4r_s in a box size ~10^5r_s, where r_s is sink size. Especially, the errors around sink ($10r_g\le r\le 50r_g$) excluding the position in which is influenced by the inner boundary, are less

than 0.3 %. The bottom right of Fig. 2 represents how precisely one can calculate the specific angular momentum with our code.

Lee et al. (2016) extended the analytical solution including scale height in one dimension to two dimensions and presented the computational results to represent the actual situation around a black hole suggested in the theory. To properly represent analytical solutions in multi-dimensional spaces, the code must be able to accurately calculate angular momentum. However, in the calculations of Igumenshchev et al. (1996), since the azimuthal momentum equation is not separated from other equations, it is difficult to separately handle the conservation of angular momentum even in the absence of viscosity. Therefore, to follow up the exact spread of the angular momentum due to viscosity, Lagrangian TVD and remap, where angular momentum is 100% conserved in the absence of viscosity, is very efficient. Figure 2 (shock-free flow) and Fig. 4 (shocked flow) from Lee et al. (2016) show how well this code follows up the analytical solutions even in multi-dimensions using scale height. These results provide that the code has strong points of being able to visually and precisely express theoretical predictions about the structure of the accretion disk around a black hole through multi-dimensional numerical calculations.

Figure 3 shows density (top left), radial velocity & sound speed (top right), pressure (bottom left), and specific angular momentum (bottom right) in pseudo-Newtonian potential. We used the same initial flow conditions as in Narayan et al. (1997) to compare them, e.g., γ=1.5, α=0.3 and f=1. The straight lines for the sound speed, the radial velocity, and the specific angular momentum are the analytical self-similar solutions, whereas the dashed line in the bottom right represents Keplerian specific angular momentum. The slopes for the density and the pressure are $r^{-\frac{3}{2}}$ and r^{-2}. As Narayan et al. (1997) suggested, the ADAFs in pseudo-Newtonian potential become supersonic flows close to the black hole. The sonic point depends on the viscosity parameter α and it becomes $5.315r_g$ especially for α=0.3. The sonic point from the numerical consequence represents around the position $r\sim5.3r_g$. The features of radial velocity, sound speed, and specific angular momentum are almost the same as in Figs. 1 and 2 of Narayan et al. (1997). Based on their Fig. 2, the specific angular momentum does not come close to the line of the analytical self-similar solution between $r\sim10^2r_g$ and 10^3r_g as in the bottom right of Fig. 3. Moreover, the point that the rotation is substantially sub-Keplerian even near the last stable orbit, $r\sim3r_g$, is also the same as in our results.

4. Summary and Discussions

This paper is treated to cover a detailed description of the development process of the code in response to the request of researchers studying the theoretical solution. The main objective of building up Lagrangian TVD and remap code was to know the precise role of viscosity in a rotating accretion flow around a black hole through numerical simulation. Our effort shows that our code can follow up the angular momentum as accurately as possible, even near the inner boundary of a black hole, overcoming improper treatment of angular momentum close to the inner boundary. As mentioned in §3, Lagrangian TVD and remap code have two strong merits: (1) the capacity to resolve shock sharply and (2) the capability of conserving 100 % of angular momenta in Eulerian equations. It can accommodate shock structures more efficiently. Moreover, it is also possible to follow up the angular momentum variation because the azimuthal momentum equation is decoupled from the rest of the equations.

The shock tube test in a one-dimensional plane parallel geometry shows that the present code has a more precise resolving capability shock structure within two to three cells. The test in rotating accretion flows with one-dimensional cylindrical geometry proves that our code simulation can follow up nicely with the analytical solution [Fig. 1 of Lee et al. (2011) and Fig. 1 of MRC96 for a comparison]. In two-dimensional cylindrical tests, the current results also produce a shock structure of which position in the equatorial

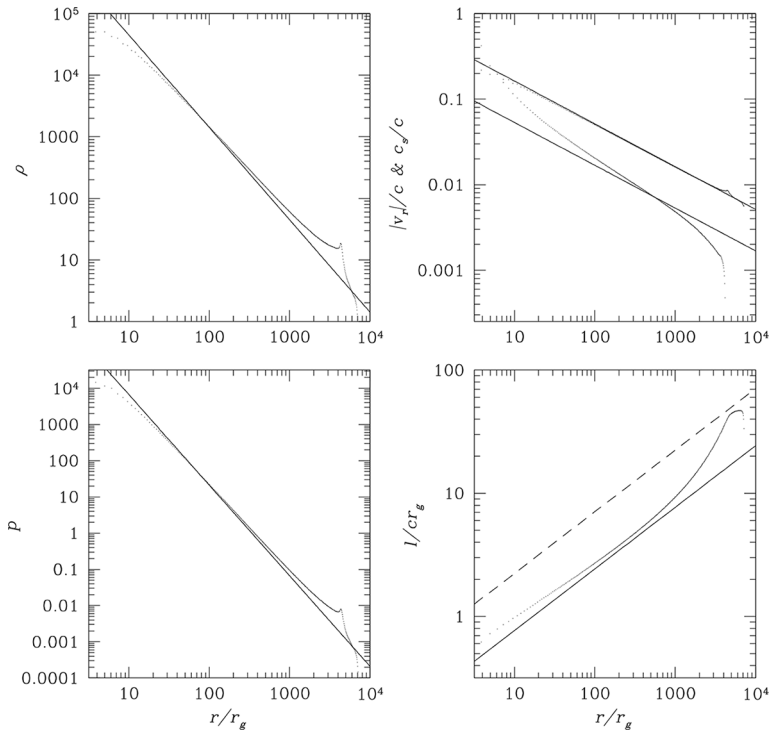

Fig. 3. Numerical results of ADAF in pseudo-Newtonian potential. The solid lines represent the analytical self-similar solutions, while the dots show the results with γ=1.5, α=0.3 and f=1. The dashed lines in the bottom right show the Keplerian specific angular momentum. Density (ρ), pressure (p), specific angular momentum (l), radial velocity (v_r) and sound speed (c_s) are shown in counterclockwise. The calculation has been performed on the 490 non-uniform grid cells with increment factor, b=1.01. The sonic point is located at the position r_{sonic}~5.3r_g.

plane is similar to the results of MRC96. Hence, since we know that the Lagrangian TVD and remap code help represent the analytical solution, our method proves beneficial in reducing the possible errors from mishandling the specific angular momentum when the viscosity is added to the simulation.

From the simulation of one-dimensional quasi-spherical geometry, including viscosity terms, we found a better result near the center, reducing the high computational time cost by employing non-uniform grids. As in Fig. 2 of Lee et al. (2011), the numerical simulation using the Newtonian potential shows excellent consequences closely matching the analytical self-similar solution. As the theoretical work might suggest, we represent that the linear, angular momenta of inflow are lost by viscosity when the flow approaches the center of the black hole. The results of Lee et al. (2016) show the role of viscosity even in multi-dimensional coordinates precisely and provide a clue to analyze various phenomena observed around black holes, such as jet and quasi-periodic oscillation (QPO).

The flow in the pseudo-Newtonian potential to mimic the general relativistic effect shows that the radial velocity is faster than the flow with the Newtonian potential. So, the flow becomes a supersonic flow near the black hole. The flow characteristics depend on the viscosity parameter α: the smaller α is, the closer the sonic point to the black hole is. The sonic point at the position r_{sonic}~5.3r_g for α=0.3 and γ=1.5 in Fig. 3 matches the earlier conclusion by Narayan et al. (1997).

Acknowledgments

We would like to acknowledge support from the National Research Foundation of Korea (NRF) grant funded by the Korea government (MSIT) (No. RS-

2023-00277151). S.-J. L. is grateful to Prof. Ryu of UNIST, who provided the original TVD code.

References

Collella, P., & Woodward, P.R., 1984, The piecewise parabolic method (PPM) for gas-dynamical simulations, Journal Computational Physics, 54, 174-201.

Godunov, S.K., 1959, Finite difference method for numerical computation of discontinuous solutions of the equations of fluid dynamics, Matematičeskij Sbornik, 47, 271-306.

Harten, A., 1983, High resolution schemes for hyperbolic conservation laws, Journal of Computational Physics, 49, 357-393.

Harten, A., Engquist, B., Osher, S., & Chakravarthy, S.R., 1987, Uniformly high order accurate essentially non-oscillatory schemes, III, Journal of Computational Physics, 71, 231-303.

Jiang, G.-S., & Shu, C.-W., 1996, Efficient implementation of weighted ENO schemes, Journal of Computational Physics, 126, 202-228.

Igumenshchev, I.V., Chen, X., & Abramowicz, M.A., 1996, Accretion discs around black holes: two-dimensional, advection-cooled flows, Monthly Notices of the Royal Astronomical Society, 278, 236-250.

Igumenshchev, I.V., & Abramowicz, M.A., 1999, Rotating accretion flows around black holes: convection and variability, Monthly Notices of the Royal Astronomical Society, 303, 309-320.

Igumenshchev, I.V., & Abramowicz, M.A., 2000, Two-dimensional models of hydrodynamical accretion flows into black holes, The Astrophysical Journal Supplement Series, 130, 463-484.

Lee, S.-J., Ryu, D., & Chattopadhyay, I., 2011, Quasi-spherical, time-dependent viscous accretion flow: one-dimensional results, The Astrophysical Journal, 728:142, 1-13.

Lee, S.-J., Chattopadhyay, I., Kumar, R., Hyung, S., & Ryu, D., 2016, Simulations of viscous accretion flow around black holes in a two-dimensional cylindrical geometry, The Astrophysical Journal, 831:33, 1-22.

LeVeque, R.J., 1998, Nonlinear Conservation Laws and Finite Volume Methods for Astrophysical Fluid Flow, 27th Saas-Fee Advanced Course Lecture Notes.

Liu, X.-D., Osher, S., & Chan, T., 1994, Weighted essentially non-oscillatory schemes, Journal of Computational Physics, 115, 200-212.

Longair, M.S., 1994, High Energy Astrophysics (London: Cambridge Univ. Press).

Molteni, D., Ryu, D., & Chakrabarti, S.K., 1996, Numerical simulations of standing shocks in accretion flows around black holes: A comparative study, The Astrophysical Journal, 470, 460-468.

Narayan, R., & Yi, I., 1994, Advection-dominated accretion: A self-similar solution, The Astrophysical Journal, 428, L13-L16.

Narayan, R., Kato, S., & Honma F., 1997, Global structure and dynamics of advection-dominated accretion flows around black holes, The Astrophysical Journal, 476, 49-60.

Ogilvie, G.I., 1999, Time-dependent quasi-spherical accretion, Monthly Notices of the Royal Astronomical Society, 306, L9-L13.

Paczynski, B., & Wiita, P.J., 1980, Thick accretion disks and supercritical luminosities, Astronomy and Astrophysics, 88, 23-31.

Press, W.H., Teukolsky, S.A., Vetterling, W.T., & Flannery, B.P., 1992, Numerical Receipes in Fortran (London: Cambridge Univ. Press).

Pringle, J.E., 1981, Accretion discs in astrophysics, Annual Review of Astronomy and Astrophysics, 19, 137-162.

Roe, P.L., 1981, Approximate Riemann solvers, parameter vectors, and difference schemes, Journal of Computational Physics, 43, 357-372.

Ryu, D., & Jones, T.W., 1995a, Numerical magnetohydrodynamics in astrophysics: algorithm and tests for one-dimensional flow, The Astrophysical Journal, 442, 228-258.

Ryu, D., & Jones, T.W., & Frank, A., 1995b, Numerical magnetohydrodynamics in astrophysics: algorithm and tests for multi-dimensional flow, The Astrophysical Journal, 452, 785-796.

Ryu, D., Yun, H.S., & Cheo, S., 1995c, A multi-dmensional magnetohydrodynamic code in cylindrical geometry, Journal of the Korean Astronomical Society, 28, 2, 223-243.

Shakura, N.L., & Sunyaev, R.A., 1973, Black holes in binary systems. Observational appearance., Astronomy and Astrophysics, 24, 337-355.

Strang, G., 1968, On the construction and comparison of difference schemes, SIAM Journal on Numerical Analysis, 5, 506-517.

Tassoul J.-L., 1978, Theory of Rotating Stars. Princeton Univ. Press, Princeton.

Van Leer, B., 1979, Towards the ultimate conservative difference scheme V. A Second-order sequel to Godunov's method, Journal of Computational Physics, 32, 101-136.

Manuscript received: August 5, 2024
Revised manuscript received: August 22, 2024
Manuscript accepted: August 22, 2024